Effects of an Inlet Vortex on the Performance of an Axial-Flow Pump

Wenpeng Zhang, Fangping Tang *, Lijian Shi *, Qiujin Hu and Ying Zhou

College of Hydraulic Science and Engineering, Yangzhou University, Yangzhou 225009, China;
18852727757@163.com (W.Z.); yzdxhqj1121@163.com (Q.H.); 18205272495@163.com (Y.Z.)
* Correspondence: tangfp@yzu.edu.cn (F.T.); yzdxslj@126.com (L.S.);
Tel.: +86-1395-1059-552 (F.T.); +86-1510-5276-995 (L.S.)

Abstract: The formation of an inlet vortex seriously restricts axial-flow pump device performance and poses a great threat to the safe and stable operation of the entire system. In this study, the change trends of an inlet vortex and its influence on an axial-flow pump are investigated numerically and experimentally in a vertical axial-flow pump device. Four groups of fixed vortex generators (VGs) are installed in front of the impeller to create stable vortices at the impeller inlet. The vortex influence on the performance of pump device is qualitatively and quantitatively analyzed. The vortex patterns at different positions and moments in the pump device are explored to reveal the vortex shape change trend in the impeller and the pressure fluctuation induced by the vortex. The reliability and accuracy of steady and unsteady numerical results are verified by external characteristics and pressure fluctuation experimental results. Results show that it is feasible to install VGs before the impeller inlet to generate stable vortices. The vortex disturbs the inlet flow fields of the impeller, resulting in significant reductions of the axial velocity weighted average angle and the axial velocity uniformity. The vortex increases the inlet passage hydraulic loss and reduces the impeller efficiency, while it only slightly affects the guide vane and outlet passage performance. The vortex causes a low-frequency pressure pulsation and interacts with the impeller. The closer the vortex is to the impeller inlet, the more significant the impeller influence on the vortex. The blade cuts off the vortex in the impeller; afterwards, the vortex follows the blade rotation, and its strength weakens.

Keywords: inlet vortex; vortex generators; axial-flow pump; computational fluid dynamics; experiment

---

1. Introduction

The annual electricity consumption of pumps accounts for approximately one-third of China's total annual electricity generation. Therefore, it is important to improve the performance of pumps for energy conservation. At present, even though China has built more than 300 large-scale low-head pumping stations, which form the backbone of the flood control and drainage engineering systems, a large number of low-head pumping stations continue to be necessary to meet the demand for the ability to resist natural disasters and promote the rapid and stable development and modernization of the economy. The safe, stable and efficient operation of the pumping station is one of the most concerning problems of designers.

Due to the advantages of a large flow, a simple structure, flexible installation and various forms, axial-flow pumps are the most common pump type used in low-head pumping stations for the fields of interbasin and regional water transfer, agricultural irrigation and drainage, and urban water supply and drainage [1]. An axial-flow pumps is a type of high-speed periodic rotating hydraulic machinery in which the interior is essentially a complex three-dimensional unsteady turbulent flow [2].

When the inflow is uniform, unstable phenomena such as channel vortices, tip clearance vortices and wake vortices occur in the pump [3,4]. Based on decades of research, a series of accepted standards (e.g., ANSI/HI 9.8 and ANSI/HI 9.6.6) have been developed by pump manufacturers and research laboratories, providing quantitative acceptance criteria for physical hydraulic models of pump intake. However, the phenomenon of an inflow vortex sometimes still occurs in an actual pumping station and aggravates the very complex flow field in the impeller, sometimes causing a surge of pressure fluctuation and aggravation of the cavitation phenomenon. This process finally leads to pump device operation instability, including intense vibration, large noise and serious efficiency reductions [5–7]. Therefore, understanding the propagation mechanism of an inflow vortex in an axial-flow pump and studying the influence of the vortex on the performance of the axial-flow pump device are necessary.

At present, research on inflow vortices in axial-flow pumps mainly focuses on two aspects: (1) The mechanism of vortex formation and (2) measures for vortex elimination. Regarding the first aspect Constantinescu and Patel [8] described the development of a computational fluid dynamics model to simulate the three-dimensional flow field in a pump intake and to study the formation of free-surface and wall-attached vortices. Shinichiro et al. [9] researched the air-entraining vortex and submerged vortex in pump sumps by simulation. They considered the effects of turbulence model, grid density and detection method on the vortices; the simulation results, using the Reynolds-averaged Navier-Stokes (RANS) equations with the shear stress transport (SST) k-ω model successfully reproduced the experimental data. Shin [10] investigated the effect of the submergence and flow rate on free surface vortices using numerical simulation. They identified the location and shape of the free surface vortices by the minimum elevation of air-water interface, air-entrained vortex length, and the volume rendering method. Concerning vortex elimination Won et al. [11] considered three types of quadrilateral submerged bars with different shapes and dimensions in the sectional areas to reduce surface vortices and cavitation. Experimental results showed that the installation of the anti-vortex device (AVD) was very effective in reducing abnormal vortices including sub-surface vortices, pre-swirls and other undesirable hydraulic phenomena. Hyung et al. [12] conducted a numerical simulation of the flow inside the sump of a pump station and analyzed the changes in flow characteristics based on the height of the AVD installation. The results show that the appropriate installation of an AVD can improve the flow characteristics, such as flow velocity and vorticity in the pump sump, and secure stable conditions for pump operation. Previous studies have made us more aware of the generation and development mechanism of vortices, and the use of various forms of vortex elimination has also improved the performance of the pump. However, because the vortex is an unstable phenomenon, in previous studies, usually generating a vortex under a special size of the inlet pool or specific operating conditions, such as controlled submergence depth of the bell mouth and appropriate high suspension. Generally, scholars divide inlet vortices into surface vortices, wall-attached vortices and bottom-attached vortices; their morphologies are shown in Figure 1. The surface vortex and wall-attached vortex positions are unfixed, and the generation time is discontinuous. The position of the bottom-attached vortex is relatively fixed, while the generation time is also discontinuous. Although vortices can be produced under certain size and working conditions, the extremely unstable spatial and time characteristics of vortices cause great difficulties in research. To quantitatively evaluate the effect of a vortex on pump performance, it is necessary to create a relatively stable vortex.

Vortex generators (VGs) are often used to control flow fields. This technique is mature in research on airfoils and heat transfer. Martin et al. [13] computed the spanwise distribution of bound circulation on a VG by integrating the pressure force along the VG height; they validated the hypothesis for predicting the vortex strength induced by a VG in wall-bounded flow. Zeng et al. [14] analyzed the combustion flow of different advanced vortices and found by numerical calculation that the performance of an advanced vortex combustor with the VG principle is significantly better than that without it.
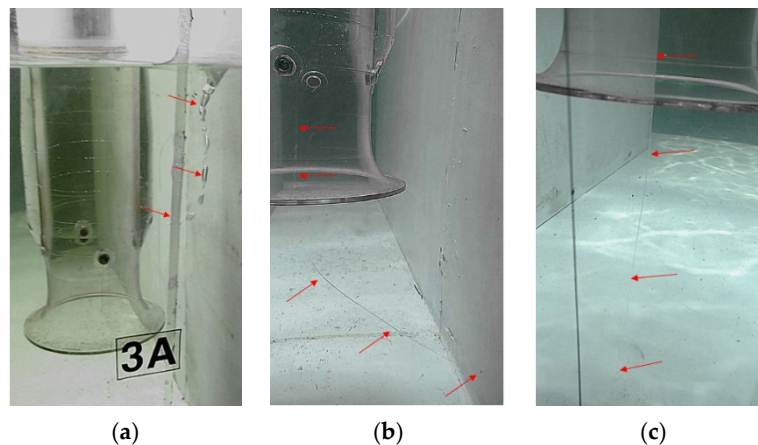
(a) (b) (c)

Figure 1. Pictures of vortices: (**a**) Surface vortex; (**b**) Wall-attached vortex; (**c**) Bottom-attached vortex.

Some scholars also apply this technology in the research of hydraulic turbines. Tian et al. [15,16] studied the application of VGs by numerical simulations and experiments based on a model draft tube. Their results show that by choosing the optimal VG parameters, such as the installation type, installation position, blade-to-blade distance, and blade inclination angle, the draft tube-equipped VGs can effectively raise the static pressure recovery coefficients and working stability. Existing research results fully show that the control effect of a VG. Therefore, to reveal the change trend of an inlet vortex and its influence on an axial-flow pump, this paper proposes installing fixed VGs in front of the impeller to generate a stable inlet flow vortex.

The remainder of this paper is organized as follows: Section 2 introduces the background of axial-flow pump devices and VGs, and the corresponding turbulence models, grid generation and numerical setup for steady and unsteady simulations are described. Section 3 presents the experimental and numerical simulation results to verify the reliability of the numerical simulation calculation. In Section 4, the numerical data with and without the VGs are discussed and compared, the influence of the vortex on the performance of the impeller and the pump device is analyzed, and the pressure fluctuation induced by the vortex is revealed. Section 5 summarizes the main results and presents the conclusions.

2. Research Object and Numerical Method

2.1. Research Object

A pump device is the core element in a pumping station. During the design of large- and medium-size pump devices, inlet passages are often adopted to provide a good inflow pattern for impellers [17]. This study is based on a vertical axial-flow pump device with an elbow inlet passage and a straight outlet passage. There are four impeller blades and seven guide vane blades. The impeller diameter in the model pump device is 0.3 m, and the rotation speed is 1450 rpm. The design flow (Q_d) of the pump device is 365 L/s. The simulation model of the axial-flow pump device is shown in Figure 2.

To generate a controllable vortex at the impeller inlet, four groups of flat plate VGs were installed at an equal distance of 0.33D from the impeller inlet. Under the design flow condition, six schemes of VG results were calculated; this study is based on one of the schemes that can produce the appropriate intensity vortex. The installation form is shown in Figure 3, and each parameter value of the VGs is shown in Table 1. The effects of the parameter values of the VGs on the strength and shape of the vortex will be studied in the future.
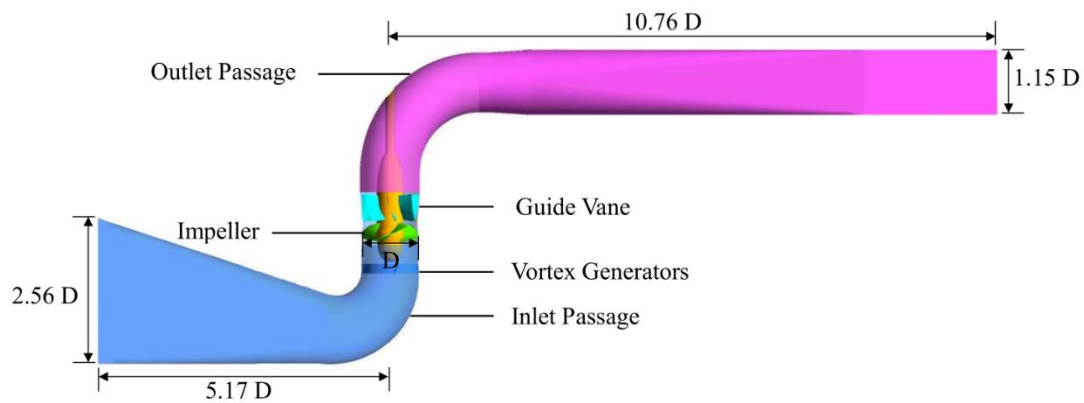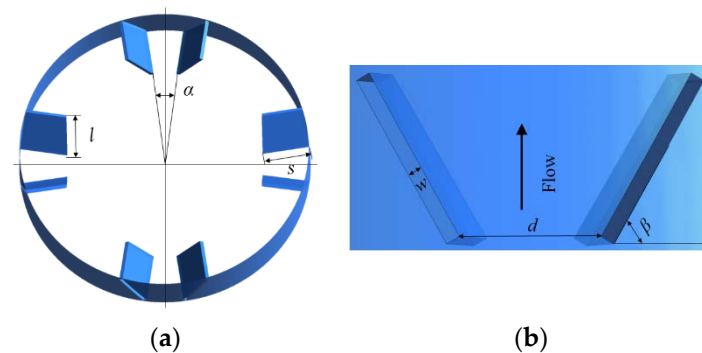
Figure 2. Layout of the vertical pump device.

Figure 3. Dimensional drawings of fixed VGs: (**a**) Top view; (**b**) Right view.

Table 1. Parameter values of the VGs.

Parameter	l (cm)	α (°)	s (cm)	w (mm)	d (cm)	β (°)
value	4	15	5	4	4	60

2.2. Numerical Simulation Method

2.2.1. Governing Equation and Turbulence Model

With the development of computer technology, an increasing number of scholars have begun to use numerical simulation methods to study pump and inflow vortices [18–20]. In this work, ANSYS CFX is utilized for the flow field calculation, and the flow is governed by the RANS equations for the numerical simulation of three-dimensional incompressible turbulent flow in pump devices.

Previous researchers have performed many studies that proved that the SST *k-ω* model improved the accuracy of turbulent flow field calculations [21–23]. In this paper, the SST *k-ω* model is applied with a better description of the vortex for simulation because it solves the boundary layer flow near the wall and the well-developed turbulent flow outside the boundary layer separately, which may simulate the flow separation better:

$$\frac{\partial(\rho k)}{\partial t} + \frac{\partial(\rho k V)_i}{\partial x_i} = \frac{\partial}{\partial x_j}\left[\left(\mu + \frac{\mu_t}{\sigma_k}\right)\frac{\partial k}{\partial x_j}\right] + P_k - \beta^* \rho \omega k \tag{1}$$

$$\frac{\partial(\rho \omega)}{\partial t} + \frac{\partial(\rho \omega V_i)}{\partial x_i} = \frac{\partial}{\partial x_i}\left[\left(\mu + \frac{\mu_t}{\sigma_\omega}\right)\frac{\partial \omega}{\partial x_j}\right] + \gamma \frac{\omega}{k} P_k - \beta \rho \omega^2 + 2(1 - F_1)\sigma_{\omega 2}\frac{\rho}{\omega}\frac{\partial k}{\partial x_j}\frac{\partial \omega}{\partial x_j} \tag{2}$$

where k is the turbulence kinetic energy; μ is the dynamic viscosity; P_k is the production term; μ_t is the turbulent eddy viscosity, which is defined in Equation (3); S is the invariant measure of the strain rate, defined in Equation (4); and F_1 is the first blending function:

$$\mu_t = \min(\frac{\rho k}{\omega}, \frac{\rho a_1 k_u}{SF_2}) \tag{3}$$

$$S = \sqrt{2E_{ij}E_{ij}}; E_{ij} = \frac{1}{2}(\frac{\partial V_i}{\partial x_j} + \frac{\partial V_j}{\partial x_i}) \tag{4}$$

All the coefficients are calculated by blending via $\alpha = F_1\alpha_1 + (1 - F_1)\alpha_2$. The model constants are: $\gamma_1 = 5/9$, $\gamma_2 = 0.44$, $\beta_1 = 0.075$, $\beta_2 = 0.0828$, $\sigma_{k1} = 1.1765$, $\sigma_{k2} = 1.0$, $\sigma_{\omega1} = 2$, $\sigma_{\omega2} = 1.168$, and $\beta^* = 0.09$.

2.2.2. Grid Division and Irrelevance Verification

The entire computing domain includes the inlet passage, vortex generators, the impeller, the guide vane and the outlet passage. According to the design parameters, to generate a three-dimensional model for the inlet passage, the guide cone and the outlet passage, and to divide the hexahedral structured grid for them using the ICEM software; the mesh growth rate of the boundary layer was 1.1. The impeller and guide vane are directly divided into structural grids in the TurboGrid software, which can automatically adapt to the span wise change in the blade shape. The impeller is the core of the pump, and a large number of studies have shown that the tip clearance and the y+ value of the grid affect the calculation accuracy directly, which has an effect on the performance of the pump [24–26]. In this paper, the tip clearance was set to 0.2 mm, and the y+ value of the wall of the impeller was calculated to be 20 in post-processing. Under the design flow condition, the efficiency of the whole pump device was verified by grid independence; the results are shown in Figure 4.
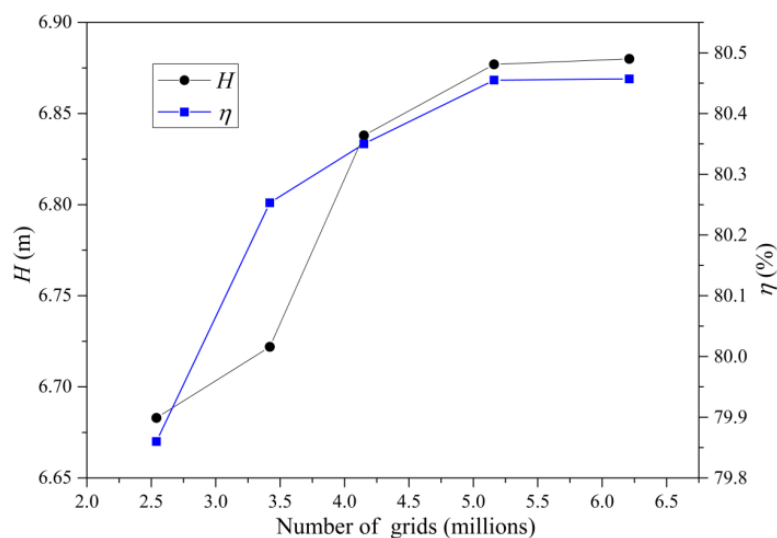

Figure 4. Analysis of grid independence for the pump device.

With an increasing number of grids, the head and efficiency of the pump device both increase. When the number of grids increases to 5.16 million, the efficiency of the pump device changes by less than 0.05%. To ensure the accuracy of the calculation and save computing resources, the final total number of grids in the computational domain was set to approximately 5.16 million. The grids of the impeller and VGs are shown in Figure 5.
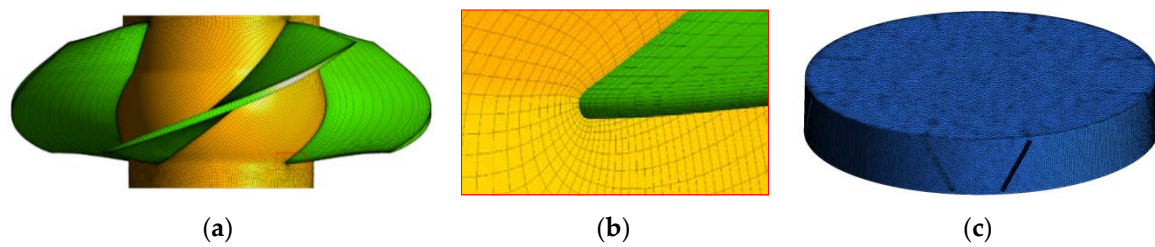
Figure 5. Figures of grids: (**a**) Impeller; (**b**) Grid refinement of impeller tip; (**c**) VGs.

2.2.3. Boundary Conditions and Monitoring Points

The entire hydraulic passage of the axial-flow pump device was first used as the steady computational domain. The pump impeller was set to the rotation domain, the rotation speed was set to 1450 rpm, and the other calculation fields were set to the stationary calculation domain. According to the actual temperature of the medium delivered in the pump device, the simulated medium was water, the water temperature was set to 25 °C, regardless of heat transfer, and the reference pressure was 1 atm. The calculated flow varied from 0.8 Q_d to 1.2 Q_d; then, the result of Q_d was taken as the initial field for the unsteady calculation. The higher-order solution format was used for the convective term, and a finite volume method was used to discretize the control equation. The coupled method was used to solve the entire numerical calculation area. The boundary conditions of the pressure inlet and the flow outlet were set. All the solid wall surfaces adopted no-slip wall conditions. The interface between the impeller rotation domain and other calculation domains was set to the dynamic-static calculation domain interface, the type was set to frozen rotor type, and the other interfaces were set to the static-static calculation domain interface. In the unsteady calculation, the impeller was rotated 2 degrees at each time step, 8 cycles were calculated, and the total time was approximately 0.331 s.

To compare the changes in the flow field in the pump before and after installation of the VGs, pressure pulsation monitoring points were set up at the inlet and outlet of the impeller; the positions of the monitoring points are shown in Figure 6.
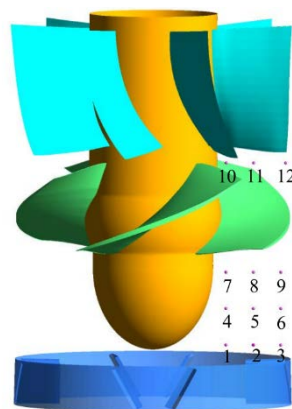

Figure 6. Location of pressure pulsation monitoring points.

3. Validation of the Numerical Simulation

The most important consideration in adopting a numerical simulation method is ensuring the accuracy of the calculation.

To verify the accuracy of the steady and unsteady numerical simulations, the external characteristics and pressure pulsation of the pump device were tested on a high-precision hydraulic mechanical test bench [27]. The comprehensive uncertainty of the test bench is ±0.39%. The test bench layout is shown in Figure 7.
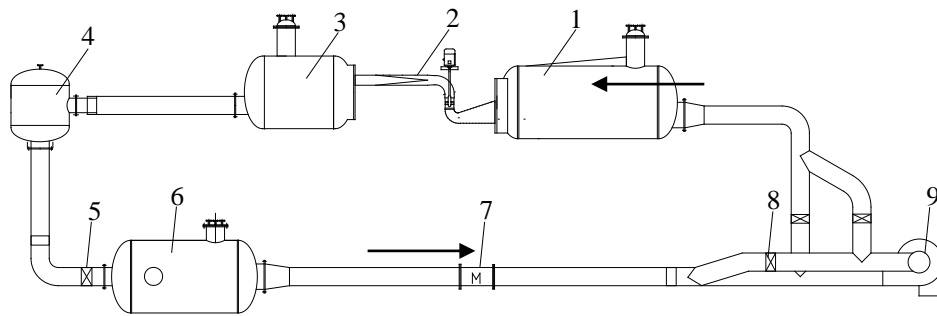
Figure 7. Layout of the experimental test system. 1. inlet tank 2. test segment schematic diagram 3. outlet tank 4. bifurcation tank 5. working condition adjustment gate valve 6. regulating rectifier 7. electromagnetic flowmeter 8. system that runs the control gate valve in forward and reverse directions 9. auxiliary pump unit.

The flow passage parts of the experiment were processed according to the size of the numerical simulation. The impeller was made of brass and was processed by computerized numerical control technology molding. The guide vane, elbow inlet passage and straight outlet passage were made of steel by welding. The models of the impeller, guide vane, VGs and pump device for the experiment are shown in Figure 8.
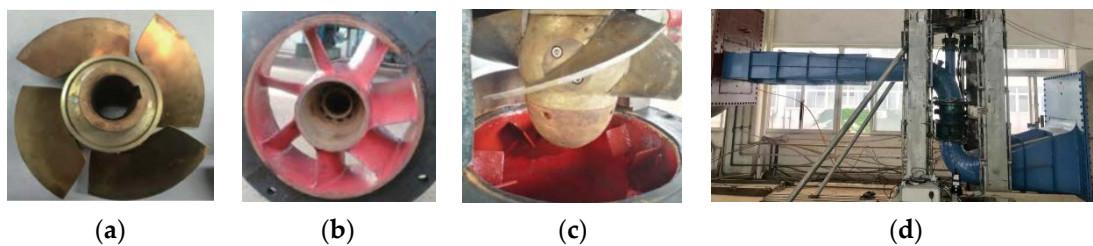

Figure 8. Picture of experiment: (**a**) Impeller; (**b**) Guide vane; (**c**) VGs; (**d**) Pump device.

In this study, the discharge was measured by an electromagnetic flowmeter (DN 400) that had an uncertainty of ±0.20%; the head was measured by a differential pressure transmitter (EJA 110A) that had an uncertainty of ±0.10%; and the shaft power was measured by a rotary torque meter (ZJ 500) that had an uncertainty of ±0.15%. The sustained data collection time was 100 s, and the collection results were processed on average. According to Equations (5) and (6), the curves of the external characteristics varying with the flow rate were obtained:

$$\eta = \frac{\rho g Q H}{N} \times 100\% \tag{5}$$

$$N = \frac{\pi}{30} n \left(M - M' \right) \tag{6}$$

where η is the efficiency of the model pump device; Q is flow rate of the model pump device; H is the head of the model pump device; ρ is the water density in the test; g is the local acceleration of gravity; N is the input power; n is rotation speed in the test; M is the input torque; and M' is the mechanical loss torque.

The comparison results of the external characteristics between the numerical simulation and experiment are shown in Figure 9.
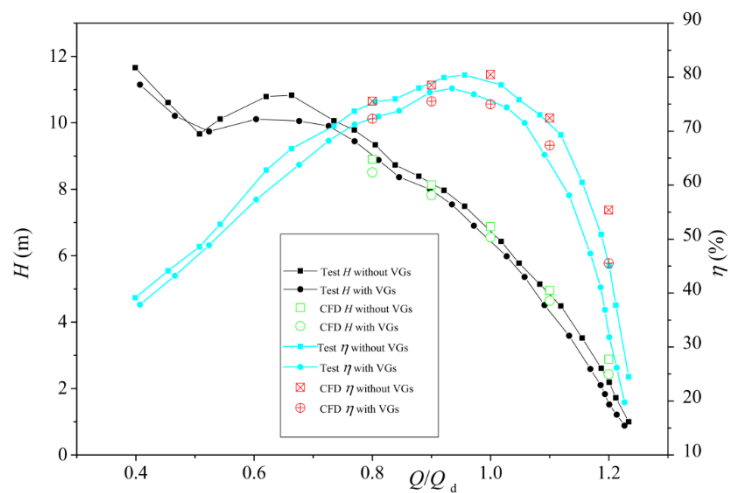
Figure 9. Comparison of the experimental and numerical simulation results.

The experimental results show that the flow-head and flow-efficiency curves with and without VGs are basically the same. With the VGs at the impeller inlet, which will directly affect the performance of the pump device, under the design flow condition, the head is reduced by approximately 0.3 m, and the efficiency is reduced by approximately 4.0%. The numerical simulation results under the design flow condition with and without VGs are all in good agreement with the experimental results, but the numerical simulation results are slightly higher than the experimental results for large flows. The reason for the error in large flows may be that the roughness of the boundary conditions for the numerical simulation and the experiment are not identical. With the increase of flow rate, the friction loss of water and side wall increase, while the head corresponding to a large flow rate is low, and the proportion of hydraulic loss is large, resulting in the calculation error for large flows. This paper mainly analyzes the variation in the vortex in the pump under design conditions and its influence on the pump performance. Therefore, the external characteristic results of the numerical simulation can be considered reliable.

With the VGs, a pressure pulsation experiment was carried out at the outlet sidewall of the impeller with a micro dynamic pressure sensor. The diameter of the measurement hole of the pressure pulsation sensor was 5 mm. The sensor has the advantages of small flow field disturbance, high sensitivity and good dynamic frequency response. The sampling frequency of the sensor was 100 kHz. The experimental data and numerical simulation results for measurement point 12 are shown in Figure 10.
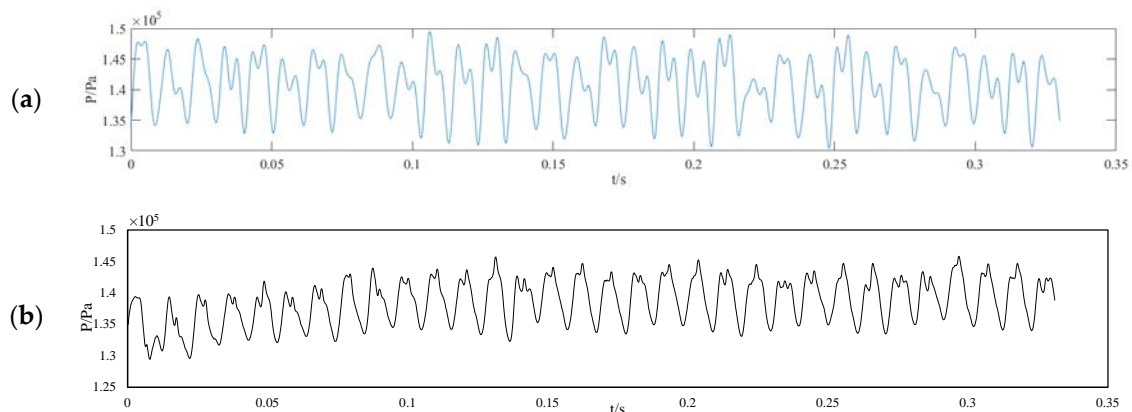

Figure 10. Time-domain diagram of pressure fluctuation: (**a**) Experiment; (**b**) Numerical simulation.

The data collected from the experiment and the data obtained from the numerical simulation were then transformed using a fast Fourier transform (FFT); and the frequency-domain diagrams are shown in Figure 11.
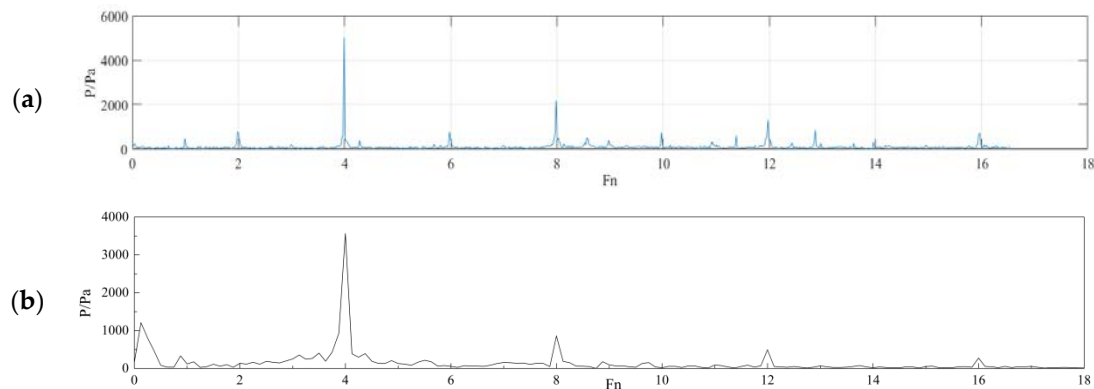

Figure 11. Frequency-domain diagram of the pressure fluctuations: (**a**) Experiment; (**b**) Numerical simulation. Fn in the figure is a multiple of the impeller rotation frequency.

The multiple frequency (*Fn*) of the impeller is defined as follows:

$$Fn = \frac{60f}{n} = \frac{f}{Fz} \tag{7}$$

where *f* is the frequency obtained by FFT and *Fz* is the impeller rotation frequency.

Figure 10 shows that the trends in the time-domain graphs for the test results and numerical simulation results are basically the same. Thirty-two peaks and troughs are observed when the impeller turns eight cycles. The values gradually increase in the first two periods, and the results then tend to be stable. In Figure 11, the frequency-domain diagrams show that the main frequency of both the numerical simulation and test results occurs at the quadruple rotation frequency because the impeller has four blades, indicating that the blade frequency at the outlet of the impeller is still the main factor affecting the pressure pulsation. The sub pulsation amplitude also appears at eight and 12 times the rotating frequency, which is caused by the dynamic and static interference between the impeller and the guide vane. The guide vane and the impeller are mutual excitation sources, resulting in these harmonics. The numerical results are lower than the experimental results, while the frequency occurrence positions are consistent. Factors such as vibration and installation error were ignored in the numerical simulation and may be the reasons for the difference in the results. Overall, the unsteady results of the numerical simulation are considered reliable.

4. Results and Discussions

4.1. The Influence of the Vortex on the Inlet Flow Field of the Impeller

Inlet flow fields have a direct effect on impeller performance. To quantitatively analyze the flow field state of the impeller inlet, the distribution uniformity of the axial velocity at the impeller inlet is denoted as $\overline{V}_u$. A modified formula is proposed that ignores the influence of the grid area on the calculation results and improves the calculation accuracy as follows:

$$\overline{V}_u = \left[1 - \frac{1}{v_a} \frac{\sum_{i=1}^{n} \Delta A \sqrt{(v_a - v_i)^2}}{A} \right] \times 100\% \tag{8}$$

$$v_a = \frac{Q}{A} \tag{9}$$

where $\overline{V}_u$ is the distribution uniformity of the axial velocity; v_a is the average axial velocity; ΔA is the calculated cell grid area; v_i is the axial velocity of the calculated cell grid; and A is the area of the calculated section.

The axial velocity weighted average angle ($\overline{\theta}$) is a common index to evaluate the angle of incidence. Its expression as follows:

$$\overline{\theta} = \frac{\sum_{i=1}^{n} v_{ai} \left[90 - \arctan\frac{v_{ti}}{v_{ai}} \right]}{\sum_{i=1}^{n} v_{ai}} \tag{10}$$

where v_{ti} is the tangential velocity at the inlet plane of the impeller. The closer $\overline{\theta}$ is to 90°, the more uniform the axial-flow velocity distribution at the inlet plane of the impeller.

Under the design flow rate, 5 measurement lines were taken before the impeller inlet to compare the differences in the radial velocity. The positions and velocities of each measurement line are shown in Figures 12 and 13. The X-coordinate value in the figure is the horizontal distance between each point and the hub center.
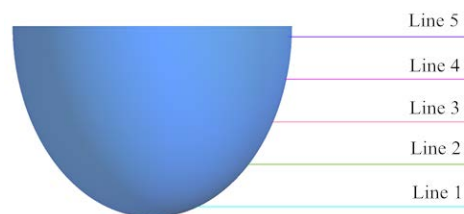

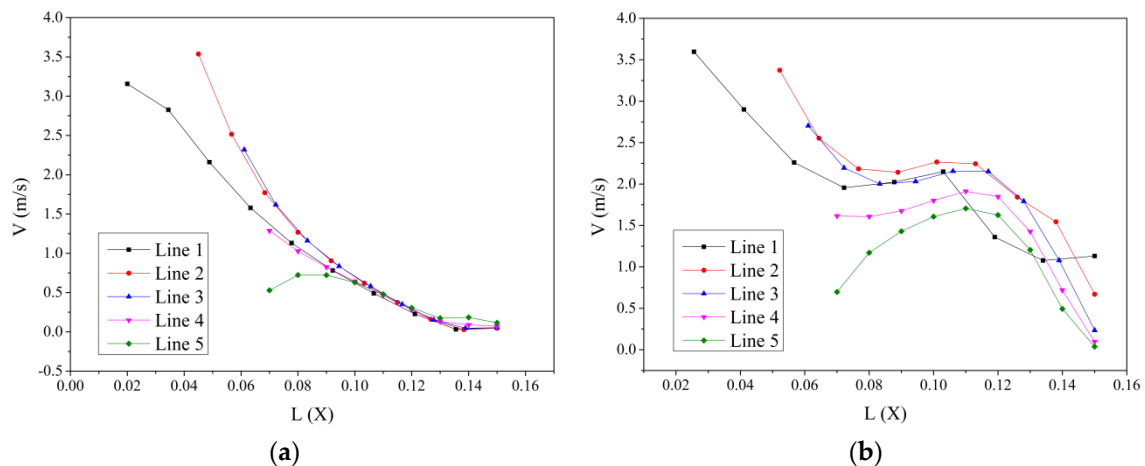**Figure 12.** Radial velocity measurement lines of the impeller inlet.

(**a**)　　　　　　　　　　(**b**)

Figure 13. Radial velocity of the impeller inlet: (**a**) Without VGs; (**b**) With VGs.

As shown in Figure 13, in the absence of VGs, the radial velocity of each measurement line gradually decreases from the hub to the shroud. In the main flow area, the radial velocity of each measurement line is basically the same, and the differences between values are small, indicating a better inlet flow pattern of the impeller. In the presence of VGs, the radial velocity of each measurement line obviously changes, and the differences between measurement lines are significant. When X = 0.11 m, the radial velocities of line 2 and line 5 increase by 1.7 m/s and 0.9 m/s, respectively. As the distance between a measurement line and the VGs increases, the intensity of the disturbance of the radial velocity decreases, which also indicates that the intensity of the vortex is decreasing.

In the inlet plane of the impeller, $\overline{\theta}$ and $\overline{V}_u$ under different flow rates were obtained, as shown in Figure 14.
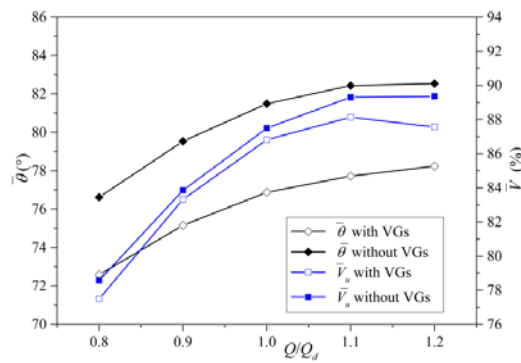
Figure 14. Comparison diagram of $\overline{V}_u$ at the impeller inlet.

As shown in Figure 14, without VGs, $\overline{\theta}$ and $\overline{V}_u$ increase with an increasing flow rate; with VGs, $\overline{\theta}$ increases with an increasing flow rate, while $\overline{V}_u$ first increases and then decreases. Overall, without VGs, the smaller the flow rate is, the flow pattern at the inlet plane is more disordered, which conforms to the characteristics of a general axial-flow pump. With VGs, the disturbance of the vortex generator to the flow state is significant, and presented the trend of the larger the flow, the more serious the disturbance. When the size of the VGs is fixed, with the increase of the flow rate, the effect of blocking water increases, the intensity of the generated vortex is stronger, and the damage to the flow field is greater.

4.2. Effect of the Vortex on the Pump Device Performance

When water passes through the flow parts, such as the inlet and outlet passages, friction, impact, vortices and backflow will occur [27]. Such losses are called the hydraulic loss, which is an important factor affecting the performance of the pump device, expressed as follows:

$$\Delta h = \left(\frac{P_1}{\rho g} - \frac{P_2}{\rho g} + Z_1 - Z_2 \right) + \left(\frac{u_1^2}{2g} - \frac{u_2^2}{2g} \right) \tag{11}$$

where P_2 is the static pressure of the outlet sections; Z_1 is the water level in the inlet sections; Z_2 is the water level in the outlet sections; u_1 is the velocity of the inlet sections; and u_2 is the velocity of the outlet sections.

For the inlet passage with VGs, the loss is mainly divided into three parts, which can be described by the following expression:

$$\Delta h_{in} = F_V + F_G + F_r \tag{12}$$

where F_V is the hydraulic loss caused by vortex turbulence; F_G is the hydraulic loss caused by the water-blocking function of the VGs; and F_r is the friction loss between the water flow and the passage wall.

The hydraulic losses for each part of the inlet passage is shown in Figure 15. With increasing flow rate, the hydraulic losses of each part of the inlet passage and the total hydraulic losses increase. Regarding the hydraulic losses of each part, F_r is closely related to the size of the inlet passage. In the optimization calculation of the inlet passage, this loss should be as small as possible, but it cannot be eliminated. F_G is the water-blocking function of the VGs and will not be produced in actual engineering. F_V is the unnecessary hydraulic loss caused by the vortex in the inlet passage and must be eliminated. After calculation, F_V. accounts for 25–30% of the total hydraulic loss in the inlet passage, and its influence othe efficiency of the pump device is 0.5–2.2%.
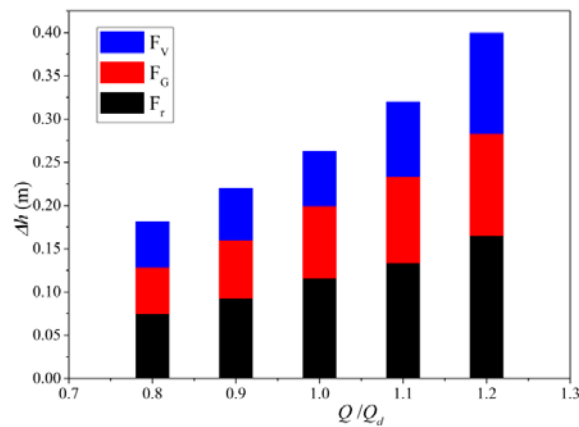
Figure 15. Diagram of hydraulic loss in the inlet passage.

The inlet flow field directly affects the impeller performance. The impeller efficiency in different working conditions with and without VGs was obtained as shown in Figure 16.
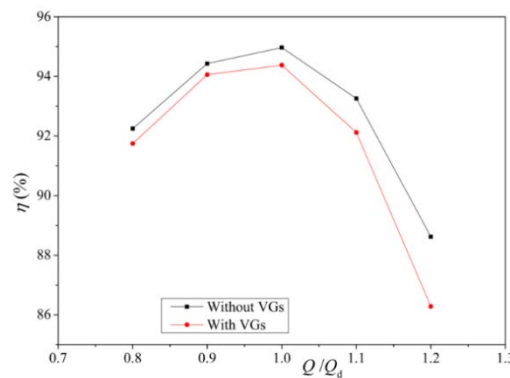

Figure 16. Comparison diagram of the impeller efficiency with and without VGs.

Figure 16 shows that the change trends of the efficiency of the two impellers with the flow rate are the same; however, with increasing flow rate, the difference between the impellers increases. The larger the flow rate is, the more serious the decrease in impeller efficiency with VGs and the greater the influence of the vortex on the performance of the impellers. According to the comparison and analysis of Figure 14, the variation trend of distribution uniformity of the axial velocity is consistent with that of the impeller efficiency. For Q_d, $\overline{V}_u$ is reduced by 0.6% and the corresponding impeller efficiency is reduced by 0.7%; for 1.2 Q_d, the value of $\overline{V}_u$ is reduced by 1.2% and the corresponding impeller efficiency is reduced by 1.8%.

The influence of the vortex on the flow patterns of the impeller, the guide vane and the outlet passage was qualitatively analyzed under the design condition. The velocity contour of the impeller center section was obtained, as is shown in Figure 17.

When no vortex occurs, the velocity distribution inside the impeller presents a stepped shape, gradually rising from the blade inlet to the outlet, and the velocity is small near the hub and large near the shroud. In the presence of a vortex, the velocity distribution in the impeller is similar to that in the absence of a vortex. The disturbance of the inlet flow field of the blade due to the vortex is evident, and this disturbance disrupts the velocity distribution in the impeller, reducing the ability of the impeller to work.
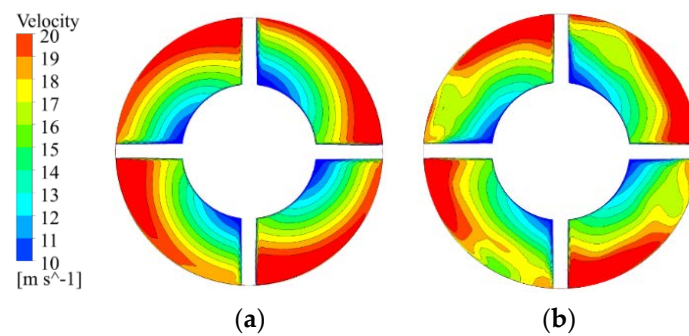
Figure 17. Velocity distribution diagram inside the impeller: (**a**) Without VGs; (**b**) With VGs.

As an important part of the pump device, the guide vane can recover the loop amount of high-speed rotating water flowing out of the impeller and convert the kinetic energy into pressure energy. The dynamic and static interactions between the impeller and the guide vane have been the focus of research [28]. After the rectification of the guide vane, the axial velocity at the outlet of the guide vane should be uniform.

Figure 18 shows that in each channel of the guide vane there is a low axial velocity zone in the back of the blades. An uneven velocity distribution and a large velocity gradient can easily cause flow instabilities. When an inlet vortex occurs, the zone of low axial velocity near the hub decreases, and a few channels appear low axial velocity near the shroud. According to Equation (8), the calculated values of $\overline{V}_u$ for Figure 18a,b are 74.5% and 76.1%, respectively. This indicates that the inlet vortex will influence the interior flow fields of the guide vane; however, the effect is limited. In addition, appropriate flow pattern interference may improve the inner backflow of the guide vane, and this effect is also worth further study.
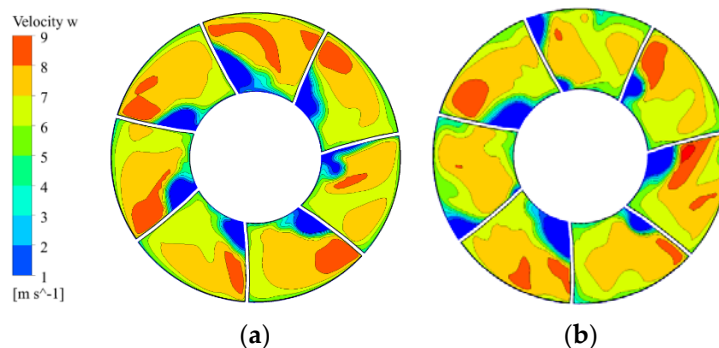

Figure 18. Axial velocity distribution diagram inside the guide vane: (**a**) Without VGs; (**b**) With VGs.

The outlet passage is an important part of the pump device, and its internal flow pattern directly affects the efficiency and stability of the pump device [29]. The pressure contour of the middle section of the outlet passage was obtained, as shown in Figure 19. The pressure cloud diagram of the outlet passage shows that the lateral pressure is high in the turn section, while the internal pressure is low. The pressure gradually increases from the inlet to the outlet of the outlet channel, indicating that the energy of the flow is converted from kinetic energy to pressure energy. The pressure distribution trends with and without an inlet vortex are basically the same, but the pressure values are slightly different, which may be caused by the different abilities of the impeller to work. The inlet vortex has little effect on the performance of the outlet passage.
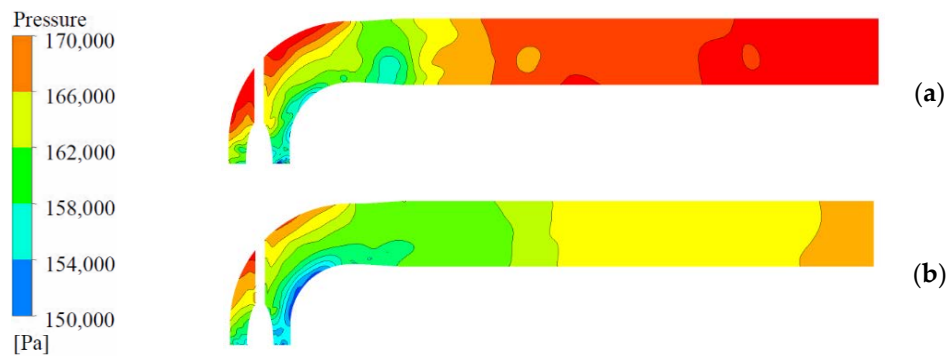
Figure 19. Outlet passage pressure distribution: (**a**) Without VGs; (**b**) With VGs.

4.3. Shape Changes of the Vortex

The pressure contour diagram, velocity vector and vortex diagram in the water guide cone were obtained under the design condition. This paper studies the vortex according to the q criterion [30,31], when $q = 6 \times 10^4$ s^{-2}, the shape of the vortex is shown in Figure 20.
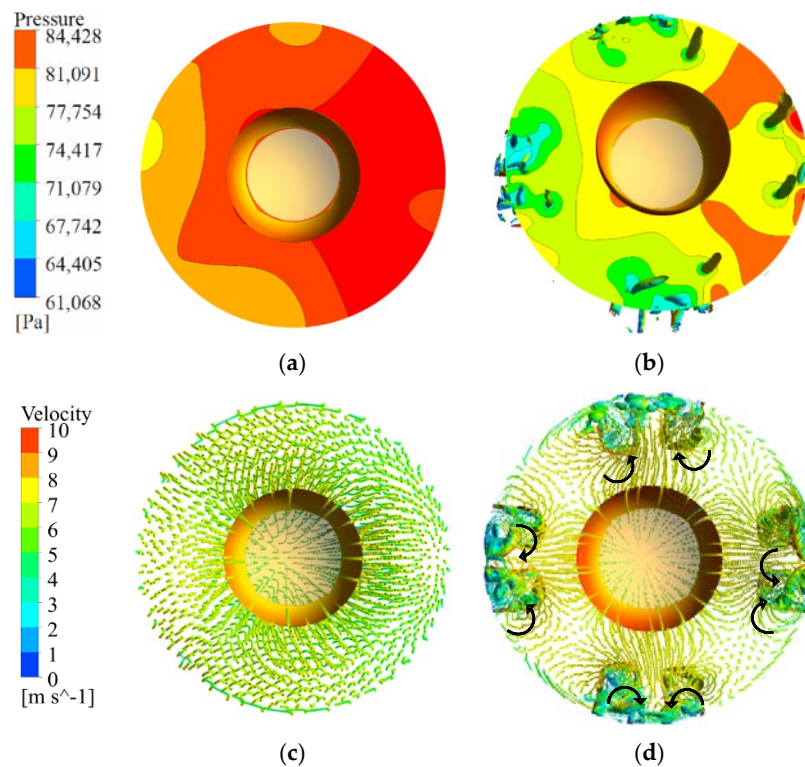

Figure 20. Inlet flow field of the impeller: (**a**) Pressure contour diagram without VGs; (**b**) Pressure contour diagram with VGs; (**c**) Velocity vector and vortex diagram without VGs; (**d**) Velocity vector and vortex diagram with VGs.

In the absence of VGs, the overall pressure of the section is high, and the pressure distribution is relatively uniform; no vortex appears. Influenced by the water guide cap, the water tends to flow from the hub to the shroud and is influenced by the blade, forming four high-speed zones. With the VGs, four pairs of counter-rotating vortices are formed in the water guide cone. A low-pressure area correspondingly occurs at the vortex positions, and the pressure distribution is uneven. Influenced by the elbow inlet passage, the shapes of the four groups of vortices are slightly different. The shapes of the vortices are greatly different on the left and right sides, and the left low-pressure area is evident. The shape of the low-pressure area at the upper and lower positions is the same as that of the vortices.

Although the VGs can produce a continuous vortex and its position is relatively fixed, the shape of the vortex will also twist due to the disturbance of the rotating blades.

Because the impeller is the core part of the pump, exploring the propagation of the vortex and its influence on the performance of the impeller is very important. When $q = 6 \times 10^4$ s^{-2}, the vortex is identified using the isosurface and the vortex surface is expressed by the velocity.

Since there are four impeller blades, an impeller rotation of 90° is identified as a cycle to analyze the change in the vortex in the impeller, as shown in Figure 21. On the suction surface side of the blade, the blade sweeps the vortex, cutting it off, and the vortex is closely attached to the blade. When the blade rotates to different angles, the vortex position remains unchanged. On the pressure surface side of the blade, after the vortex is cut off by the blade, the shape of the vortex is destroyed, the strength of the vortex is weakened, and the vortex tends to follow the movement of the blade.
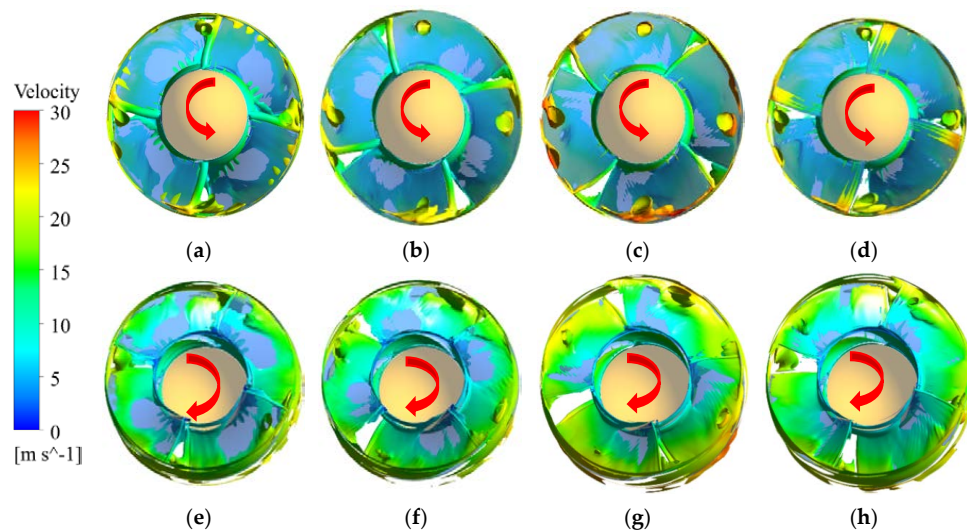

Figure 21. The internal vortex shape of the impeller at different moments: (**a**–**d**) See from the direction of the impeller inlet that the blades rotate counterclockwise; they are rotated by 0°, 30°, 60° and 90°, respectively; (**e**–**h**) See from the direction of the impeller outlet that the blades rotate clockwise; they are also rotated by 0°, 30°, 60° and 90°, respectively.

To analyze the vortex inside the impeller more intuitively, when $q = 6 \times 10^4$ s^{-2}, the vortex is identified by the isosurface. The vortex in a single channel is shown in Figure 22 as an example.

Figure 22. Shape of the vortex in the impeller.

Figure 22 shows the shape of the vortex in the impeller. As the impeller rotates at a constant speed, the position of the vortex entering the impeller remains the same, and the vortex is cut into two parts by the impeller. The two resulting vortices remain in the shape of straight pipes. The vortex near the pressure surface moves forward a certain distance with the rotating blade, where the longer the blades sweep through the vortex, the greater that certain distance. The vortex on the suction side clings to the blade surface, and the vortex at the tail is broken up, while the vortex at the bottom is still tubular. When a blade passes by, the vortex will connect for a short time, and then be cut off by the next blade.

4.4. Vortex-Induced Pressure Fluctuation

The frequency-domain diagrams of pressure pulsation at inlet points 1, 2, 3, 7, 8, and 9 and outlet points 10, 11, and 12 of the impeller were obtained under the design flow condition, as shown in Figure 23.
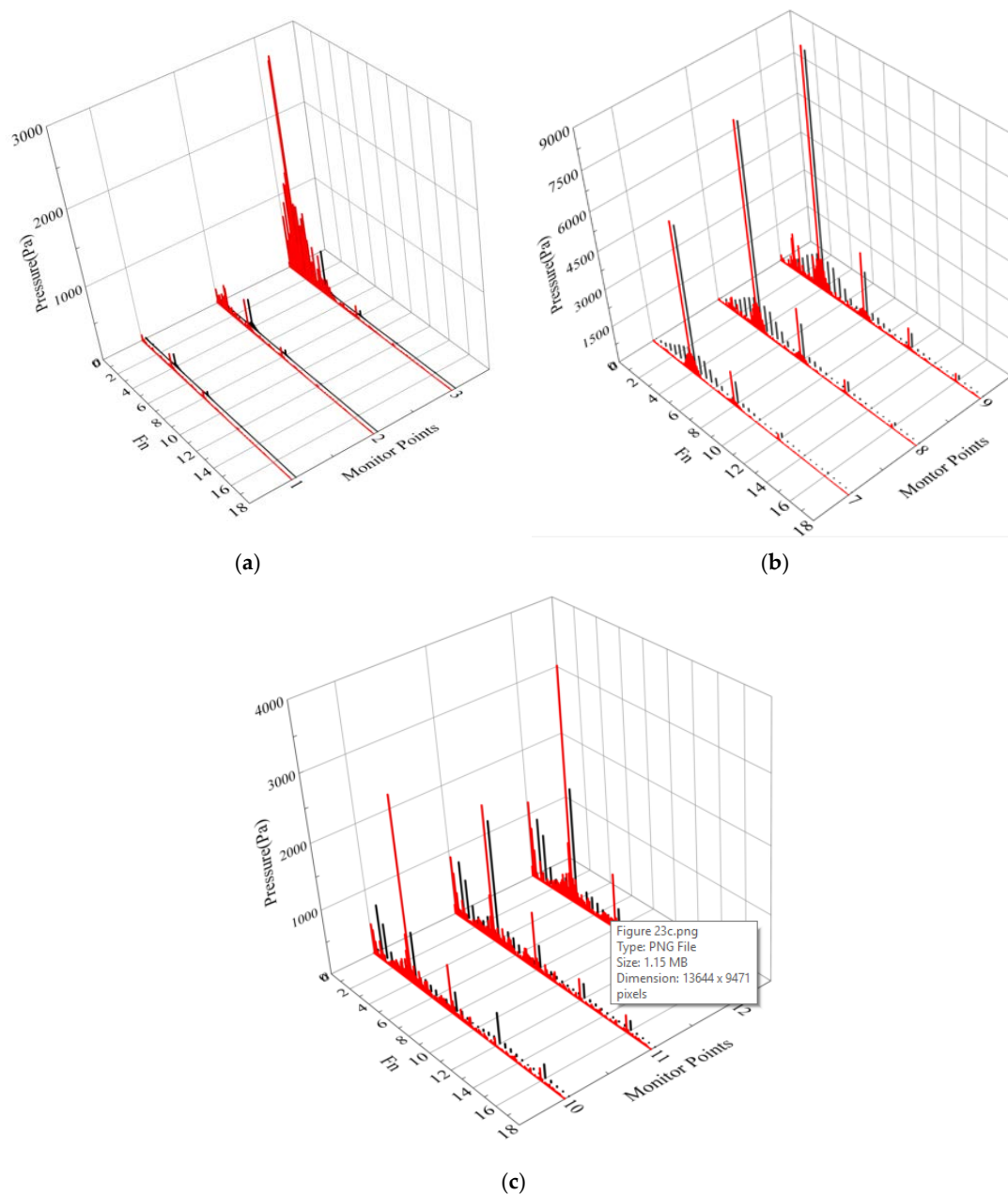

(a)

(b)

(c)

Figure 23. Comparison of the pressure fluctuation at different monitoring points: (**a**) Points 1, 2, and 3; (**b**) Points 7, 8, and 9; (**c**) Points 10, 11, and 12. In these figures, black represents the pressure pulsation without VGs, and red represents the pressure pulsation with VGs.

As shown in Figure 23a, the amplitude of the pressure fluctuation increases from the hub to the shroud. Without VGs, the main frequencies of the three measurement points are all the blade frequency, and the maximum amplitude of point 3 is 542 Pa. With VGs, the result of point 1 is the same as that without VGs. At point 2, the low-frequency pulsation with an amplitude near that of the blade frequency is increased. At point 3, the dominant frequency caused by the vortex is not the blade frequency but the rotating frequency of the impeller, and the maximum amplitude is 2870 Pa,

which is 5.3 times the amplitude without VGs. When the low-frequency pressure pulsation caused by the vortex is consistent with the vibration of the unit, it will threaten the stable operation of the pump device. As shown in Figure 23b, the main frequency is the blade frequency, and the pulsation amplitudes at measurement points 7, 8 and 9 are significantly larger than those at measurement points 1, 2 and 3. The main frequencies are all the blade frequency, and the values are the same. At point 9, with VGs, low-frequency pulsations still appear, but the amplitude is smaller, only one-fifth of the blade frequency amplitude. As shown in Figure 23c, the main frequencies of the three measurement points are still the blade frequency, and they all have low-frequency pulsations. At point 10, the main frequency with VGs is four times that without VGs. At point 11, the main frequency with VGs is nearly the same as that without VGs. At point 12, the main frequency with VGs is two times that without VGs. The above analysis shows that the pressure pulsation amplitude at the impeller inlet is larger closer to the blade position. At the outlet of the impeller, the main frequency amplitude of the pressure pulsation decreases, but the low-frequency pressure pulsation increases, which indicates that the interference effects of the rotor and the stator are strengthened and that the internal flow field becomes complicated. The above phenomenon is in accord with the general regularity of axial-flow pump pressure pulsation.

Because the low-frequency pressure fluctuation is evident near the impeller inlet sidewall, the time-domain diagrams at measurement points 3, 6 and 9 with and without VGs were obtained, as shown in Figure 24.
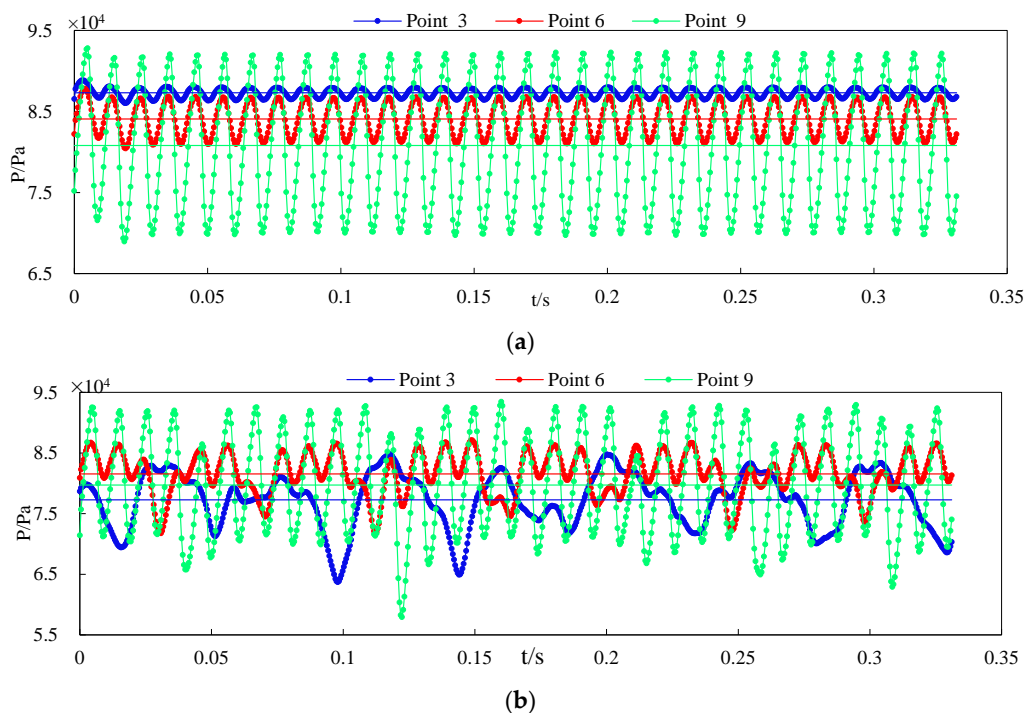

(a)

(b)

Figure 24. Time-domain diagram of the impeller inlet monitoring points: (**a**) Without VGs; (**b**) With VGs.

As shown in Figure 24a, without VGs, the pressures at these three measurement points change uniformly with time. The peaks and troughs generated by the passage of blades occur at the same times. The average pressures of monitoring points 3, 6 and 9 are 87,300 Pa, 84,075 Pa and 80,794 Pa, respectively, and the differences between the pressure trough minimum and the average value are 1282, 3645 and 11,860 Pa, respectively. The average pressure difference between point 6 and point 3 is 3225 Pa, while the average pressure difference between point 9 and point 6 is 3281 Pa; the two values are nearly equal. The amplitudes of the three points vary greatly. The amplitude of point 6 is 2.7 times that of point 3, and the amplitude of point 9 is 3.3 times that of point 6. When a measurement

point is closer to the impeller inlet, the average pressure of the measurement point is smaller, and the amplitude of the pressure fluctuation is larger. As shown in Figure 24b, with VGs, the pressure is lower because the velocity is higher at the back of the VGs, obviously; this change is caused by more than the increase of velocity because the changes in the pressures at these three measurement points with time are complex. At point 3, the shapes of the peaks and troughs are not symmetric. The peak and trough values in different periods are also very different. At points 6 and 9, the pressure changes more regularly than at point 3. The average pressures of monitoring points 3, 6 and 9 are 77,286 Pa, 81,559 Pa and 79,724 Pa, respectively, and the differences between the pressure trough minimum and the average value are 13,603 Pa, 9794 Pa and 21,975 Pa, respectively. The average pressure values of points 3, 6 and 9 first increase and then decrease, and the amplitudes of the pressure fluctuation first decrease and then increase. Comparing the two figures, with VGs, the amplitudes of the pressure fluctuation at the three points are 10.6, 2.7 and 1.8 times those without VGs. The influence of the vortex on the amplitude of the pressure fluctuation is weakened as the position of a measurement point approaches the inlet of the impeller. Additionally, the minimum pressure and the maximum pressure fluctuation amplitude occur at measurement point 9. The closer the impeller is to the inlet, the more dangerous the pressure pulsation caused by the vortex will be to the stable operation of the axial-flow pump device.

Considering that the pressure fluctuation of a monitoring point may be related to the vortex position, along with Figures 23 and 24, the vortex diagram for $q = 6.0 \times 10^4$ s^{-2} was obtained, as shown in Figure 25. To verify this conjecture, three monitoring points 3', 6' and 9' were added inside the vortex, and the Z-axis coordinates of these three points correspond to those of points 3, 6 and 9, respectively. The positions of the points relative to the vortex are also shown in Figure 25. The VGs produces a lot of very disordered vortices, but they are not fully displayed due to their low intensity. In addition, many vortices disappeared before they entered the impeller but the disturbance of the convection field does not disappear. Because this paper focuses on the interaction between the vortices and the impeller, the mechanism of the VGs is not studied in depth here.
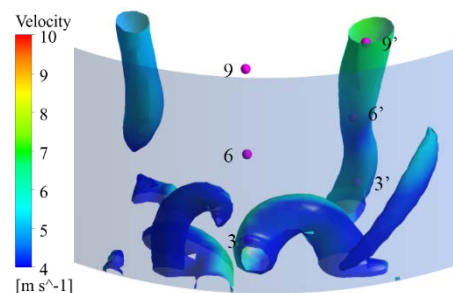

Figure 25. Positions of the vortex and monitoring points.

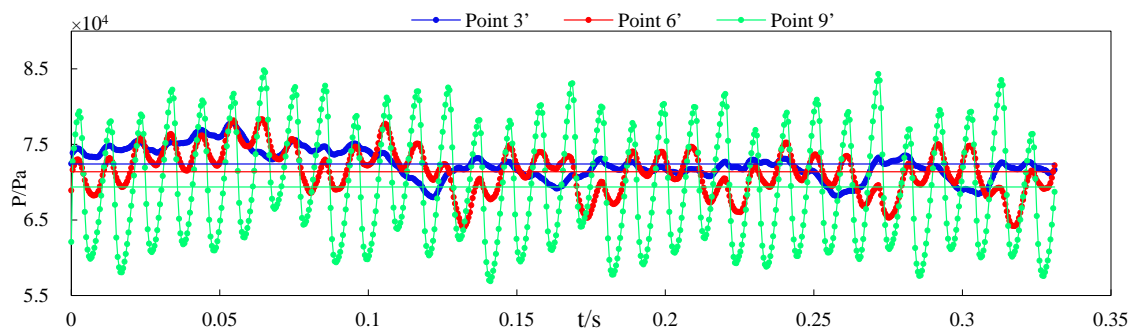The pressure fluctuations at points 3', 6' and 9' were obtained, as shown in Figure 26.

Figure 26. Pressure fluctuation in the vortex.

As shown in Figure 26, at point 3′, the pressure greatly varies in different calculation periods, and a superposition of large and small wave periods occurs. At point 6′, 32 peaks and troughs can be distinguished, but some average values are not between the peaks and troughs. At point 9′, the effect of the blade on the pressure fluctuation is very strong; however, differences still exist between the peak and trough values. As a measurement point moves toward the impeller, the pressure fluctuation at that point significantly increases, indicating that the pressure pulsation caused by the vortex is lower than that caused by the impeller.

To quantitatively analyze the pressure fluctuations induced by the vortex, the results at points 3′, 6′ and 9′ are shown in Figure 27, where the pressure with VGs is less than that without VGs.
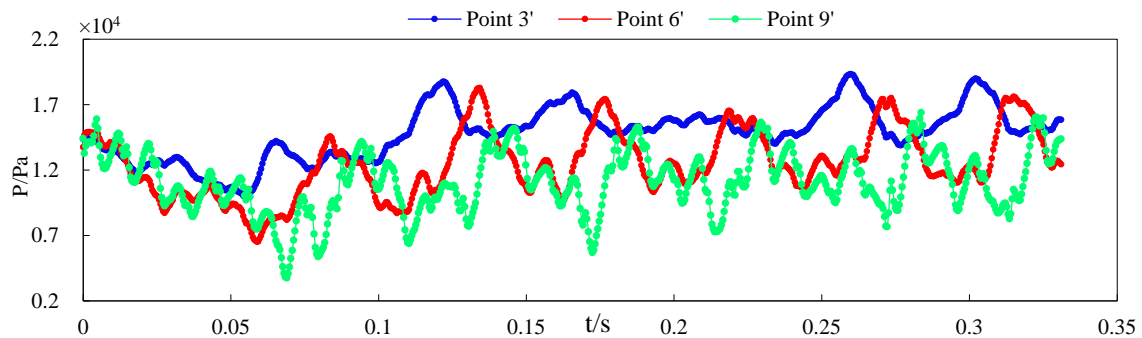

Figure 27. Time-domain diagram of vortex-induced pressure fluctuation.

As shown in Figure 27, large periodic fluctuations occur in the pressures at the three points. As the position of a measurement point moves toward the impeller, the absolute value of the pressure fluctuation caused by the vortex decreases, and peaks and troughs influenced by the blades gradually appear. The data shown in Figure 27 were transformed by the FFT method, and the frequency-domain diagram is shown in Figure 28.
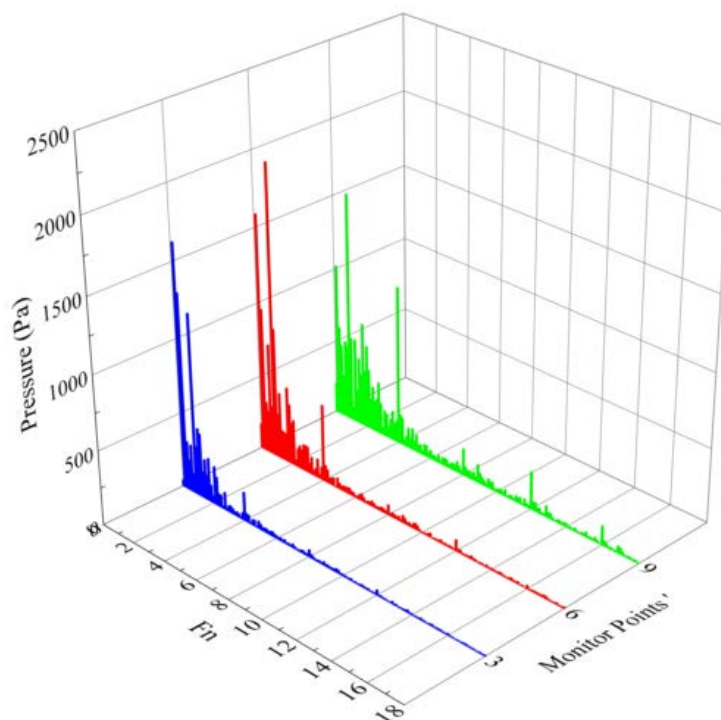

Figure 28. Frequency domain diagram of vortex-induced pressure fluctuation.

As shown in Figure 28, the amplitudes at 0–1 times the rotation frequency caused by the vortex are larger. The maximum values at points 3′, 6′ and 9′ are 1632 Pa, 1961 Pa and 1547 Pa, respectively. When a measurement point is closer to the impeller, the blade frequency of the pressure fluctuation caused by the vortex significantly increases, and the number of low-frequency pressure fluctuations is greater. The vortex at the inlet can be inferred to interact with the impeller; although the intensity of the vortex weakens near the impeller, the influence of the impeller rapidly increases.

5. Conclusions

In this work, the authors presented and discussed the performance of an axial-flow pump device effected by an inlet vortex. Because the emerge time of the vortex is not continuous, and the location of the vortex is not fixed, this paper reports on a method of producing a stable inlet vortex and its effects on an axial-flow pump device. The accuracy of steady and unsteady numerical simulations is verified by external characteristic and pressure pulsation experiments. The following main conclusions are obtained through comparative analysis the results with and without the VGs.

The effect of VGs on the flow pattern of all flow path components is analyzed. The inlet vortex reduces the distribution uniformity of the axial velocity and increases the radial velocity at the inlet of the impeller. The variation trend of $\overline{V}_u$ is consistent with the impeller efficiency; it is reasonable to use the $\overline{V}_u$ as a quantitative evaluation of the inlet flow pattern. The influence of the vortex on the inlet passage performance corresponds to approximately 0.5–2.2% of the pump head, 0.4–2.3% of the impeller efficiency, and less of the guide vane and outlet passage performance. This method is feasible to study the effect of a vortex on the performance of an axial-flow pump by installing VGs at the inlet of the impeller.

The shape changes of the vortex inside the impeller are revealed. The turbulence intensity of the vortex flow field increases with increasing flow rate. With the rotation of the impeller, the blade cuts off the vortex, and the position of the front part of the vortex is stable. After being cut off, the vortex is weakened as the blade rotates. The vortex can also induce the impeller inlet to produce pressure pulsations at 0–1 times the rotation frequency, and these pulsations pose a threat to the stable operation of the pump device. The change in pressure is closely related to the location of the monitoring points. The inflow vortex interacts with the impeller; although the intensity of the vortex weakens near the impeller, the influence of the impeller rapidly increases.

Conflicts of Interest: The authors declare no conflicts of interest.

Nomenclature

A	area of the calculated section (m^2)
F_G	hydraulic loss caused by the water-blocking function of the vortex generators (m)
F_r	friction loss between the water flow and passage wall (m)
F_V	hydraulic loss caused by vortex turbulence (m)
Fz	impeller rotation frequency (Hz)
f	frequency obtained by FFT (Hz)
g	local acceleration of gravity (m/s^2)
H	head of model pump device (m)
k	turbulence kinetic energy (m^2/s)
M	input torque (N·m)
M'	mechanical loss torque (N·m)
N	input power (W)
n	rotation speed of test (r/min)
P	flow field pressure (Pa)
$P1$	static pressure of the inlet sections (Pa)
$P2$	static pressure of the outlet sections (Pa)
Pk	production term
Q	flow rate of the model pump device (L/s)
q	criterion for strength determination of the vortex (s^{-2})
S	invariant measure of the strain rate
$u1$	velocity of the inlet sections (m/s)
$u2$	velocity of the outlet sections (m/s)
$\overline{V}_u$	distribution uniformity of the axial velocity (%)
v	inflow velocity (m/s)
v_a	average axial velocity (m/s)
v_i	axial velocity of the calculated cell grid (m/s)
$Z1$	water level in the inlet sections (m)
$Z2$	water level in the outlet sections (m)
ΔA	calculated cell grid area (m2)
Δh	hydraulic loss of flow parts (m)
μ	fluid dynamic viscosity (m2/s)
μt	turbulent eddy viscosity (m2/s)
η	efficiency of the model pump device (%)
ρ	water density at test (kg/m3)
$\overline{\theta}$	axial velocity weighted average angle (°)

References

1. Xie, C.; Tang, F.; Zhang, R.; Zhou, W.; Zhang, W.; Yang, F. Numerical calculation of axial-flow pump's pressure fluctuation and experiment analysis. *Adv. Mech. Eng.* **2018**, *10*, 1–13. [CrossRef]
2. Feng, J.; Luo, X.; Guo, P.; Wu, G. Influence of tip clearance on pressure fluctuations in an axial flow pump. *J. Mech. Sci. Technol.* **2016**, *4*, 1603–1610. [CrossRef]
3. Laborde, R.; Chantrel, P.; Mory, M. Tip clearance and tip vortex cavitation in an axial flow pump. *J. Fluids Eng.* **1997**, *119*, 680–685. [CrossRef]
4. Shi, L.; Zhang, D.; Jin, Y.; Shi, W.; van Esch, B.P.M. A study on tip leakage vortex dynamics and cavitation in axial-flow pump. *Fluid Dyn. Res.* **2017**, *3*, 1–19. [CrossRef]
5. Tang, X.; Wang, F.; Li, Y.; Cong, G.; Shi, X.; Wu, Y.; Qi, L. Numerical investigations of vortex flows and vortex suppression schemes in a large pumping-station sump. *Proc. Inst. Mech. Eng. C J. Mech. Eng. Sci.* **2011**, *225*, 1459–1480. [CrossRef]
6. Zhan, J.; Wang, B.; Yu, L.; Li, Y.; Tang, L. Numerical investigation of flow patterns in different pump intake systems. *J. Hydrodyn.* **2012**, *6*, 873–882. [CrossRef]
7. Song, X.; Liu, C. Experimental investigation of floor-attached vortex effects on the pressure pulsation at the bottom of the axial flow pump sump. *Renew. Energy* **2020**, *145*, 2327–2336. [CrossRef]

8. Constantinescu, G.S.; Patel, V.C. Numerical Model for Simulation of Pump-Intake Flow and Vortices. *J. Hydraul. Eng.* **1998**, *2*, 123–134. [CrossRef]

9. Shinichiro, Y.; Ryo, Y.; Toshinori, K.; Shunsuke, H.; Yasunori, N.; Shunji, H.; Toshihiko, K.; Toshihiro, T. Numerical study of air-entraining and submerged vortices in a pump sump. In Proceedings of the 29th IAHR Symposium on Hydraulic Machinery and Systems, Kyoto, Japan, 16–21 September 2018.

10. Shin, B. Effect of submergence and flow rate on free surface vortices in pump sump. *Int. J. Fluid Mech. Res.* **2018**, *3*, 225–236. [CrossRef]

11. Won, T.; Byeong, R.; Doeg, H. An effective shape of floor splitter for reducing sub-surface vortices in pump sump. *J. Mech. Sci. Technol.* **2014**, *1*, 175–182. [CrossRef]

12. Hyung, J.; Sung, W.; Dong, S. Numerical Analysis of the Effects of Anti-Vortex Device Height on Hydraulic Performance of Pump Sump. *KSCE J. Civ. Eng.* **2017**, *4*, 1484–1492. [CrossRef]

13. Hansen, M.O.L.; Charalampous, A.; Foucaut, J.-M.; Cuvier, C.; Velte, C.M. Validation of a Model for Estimating the Strength of a Vortex Created from the Bound Circulation of a Vortex Generator. *Energies* **2019**, *14*, 2781. [CrossRef]

14. Zeng, Z.; Du, P.; Wang, Z.; Li, K. Combustion flow in different advanced vortex combustors with/without vortex generator. *Aerosp. Sci. Technol.* **2019**, *86*, 640–649. [CrossRef]

15. Xiaoqing, T.; Yuan, Z.; Huachen, P.; Bin, S. Numerical and Experimental Study on a Model Draft Tube with Vortex Generators. *Adv. Mech. Eng.* **2013**, *5*, 509314. [CrossRef]

16. Tian, X.; Pan, H.; Hong, S.; Zheng, Y. Improvement of hydro-turbine draft tube efficiency using vortex generator. *Adv. Mech. Eng.* **2015**, *7*, 168781401559533. [CrossRef]

17. Yuan, B.; Wei, M.; Mei, Q.; Qiu, W. Analysis and Optimization of Flow Pattern in Inlet Passage of Pumping Station. *Appl. Mech. Mater.* **2011**, *130–134*, 2485–2488. [CrossRef]

18. Si, Q.; Bois, G.; Liao, M.; Zhang, H.; Cui, Q.; Yuan, S. A Comparative Study on Centrifugal Pump Designs and Two-Phase Flow Characteristic under Inlet Gas Entrainment Conditions. *Energies* **2019**, *1*, 65. [CrossRef]

19. Shi, L.; Zhu, J.; Tang, F.; Wang, C. Multi-Disciplinary Optimization Design of Axial-Flow Pump Impellers Based on the Approximation Model. *Energies* **2020**, *4*, 779. [CrossRef]

20. Gattoronchieri, A.; Cravero, C.; De, L. The application of CFD to vortical flow structures detection in sea water pumping stations. In Proceedings of the VI International Conference on Computational Methods in Marine Engineering (MARINE 2015), Rome, Italy, 15–17 June 2015; pp. 919–930. [CrossRef]

21. Menter, F.R. Two-equation eddy-viscosity turbulence models for engineering applications. *AIAA J.* **1994**, *32*, 1598–1605. [CrossRef]

22. Kim, C.; Kim, B.; Bang, B.; Lee, Y. Experimental and CFD analysis for prediction of vortex and swirl angle in the pump sump station model. In *IOP Conference Series Materials Science and Engineering, the Proceedings of International Symposium of Cavitation and Multiphase Flow (ISCM 2014), Beijing, China, 18–21 October 2014*; IOP Publishing Ltd.: Bristol, UK, 2015; pp. 1–6. [CrossRef]

23. Luo, X.; Ye, W.; Huang, R.; Wang, Y.; Du, T.; Huang, C. Numerical investigations of the energy performance and pressure fluctuations for a waterjet pump in a non-uniform inflow. *Renew. Energy* **2020**, *153*, 1042–1052. [CrossRef]

24. Zierke, W.C.; Straka, W.A. Flow visualization and the three-dimensional flow in an axial-flow pump. *J. Propuls. Power* **1996**, *2*, 250–259. [CrossRef]

25. Salim, M.; Cheah, S. Wall y+ Strategy for Dealing with Wall-bounded Turbulent Flows. *Lect. Notes Eng. Comput. Sci.* **2009**, *1*, 2165–2170.

26. Zhang, D.; Shi, L.; Chen, J.; Pan, Q.; Shi, W. Experimental analysis on characteristic of cavitation in tip region of axial flow pump impeller. *J. Zhejiang Univ. (Eng. Sci.)* **2016**, *8*, 1585–1592. [CrossRef]

27. Shi, L.; Zhang, W.; Jiao, H.; Tang, F.; Wang, L.; Sun, D.; Shi, W. Numerical simulation and experimental study on the comparison of the hydraulic characteristics of an axial-flow pump and a full tubular pump. *Renew. Energy* **2020**, *153*, 1455–1464. [CrossRef]

28. Pei, J.; Meng, F.; Li, Y.; Yuan, S.; Chen, J. Effects of distance between impeller and guide vane on losses in a low head pump by entropy production analysis. *Adv. Mech. Eng.* **2016**, *11*, 1–11. [CrossRef]

29. Guo, J.; Chen, H.; Lu, J. Numerical method for simulation of three dimensional flow in outlet passage of pump station. *Prog. Exp. Comput. Mech. Eng.* **2003**, *243*, 237–242. [CrossRef]

30. Zhang, Z.; Che, X.; Nie, W.; Li, J.; Zheng, T.; Li, L.; Chen, Q.; Zheng, Z. Study of vortex in flow fields induced by surface dielectric barrier discharge actuator at low pressure based on Q criterion. *Plasma Sci. Technol.* **2018**, *1*, 1–6. [CrossRef]

31. Zhang, Y.; Wang, X.; Zhang, Y.; Liu, C. Comparisons and analyses of vortex identification between Omega method and Q criterion. *J. Hydrodyn.* **2019**, *2*, 224–230. [CrossRef]